



# Mechanical and microstructural features of wire-and-arc additively manufactured carbon steel thick plates

Vittoria Laghi<sup>1</sup> · Lidiana Arrè<sup>1</sup> · Lavinia Tonelli<sup>2</sup> · Gianluca Di Egidio<sup>2</sup> · Lorella Ceschini<sup>2</sup> · Ivan Monzón<sup>3</sup> · Alberto Laguía<sup>3</sup> · José Antonio Dieste<sup>3</sup> · Michele Palermo<sup>1</sup>

Received: 7 December 2022 / Accepted: 4 May 2023 / Published online: 26 May 2023  
© The Author(s) 2023

## Abstract

Metal additive manufacturing (AM), in particular wire-and-arc additive manufacturing (WAAM), has become over the last few years the breakthrough technology to reduce the environmental impact and increase the efficiency of steel structures. Although intense research effort has been paid toward the mechanical characterization of WAAM-produced thin walls, little attention has been devoted to the investigation of multi-layered thick parts. These latter would indeed expand the application of WAAM for large-scale constructions requiring thicker cross-sections to withstand high loading conditions. The present work provides a comprehensive experimental investigation of mild steel WAAM thick plates from the fabrication to the mechanical and microstructural characterization. First, the fabrication process is presented in full details. From that, microstructural and mechanical characterization is described and discussed, showing a homogeneous microstructure with little influence on the mechanical response along the wall plate thickness, also considering different specimen orientations with respect to the printing directions. The results confirm good mechanical properties of the printed outcomes, in line with those of structural mild steels manufactured with conventional technologies. Little influence on the response along the thickness is reported, thus proving the required quality of WAAM thick parts for applications in the construction sector.

**Keywords** Additive manufacturing · Wire-and-arc · Mild steel · Thick plates · Microstructural analysis · Mechanical characterization

## 1 Introduction

Current strategies for the realization of automated steel constructions see the application of metal additive manufacturing (AM) processes, and in particular wire-and-arc additive manufacturing (WAAM), as an opportunity to build a new generation of efficient steel structures with reduced material use. This, though, does require advanced multidisciplinary knowledge in manufacturing, metallurgy, structural engineering and computational design.

The digitalization of the construction sector could potentially produce more efficient structures, reduce material waste, and increase work safety [1, 2]. Moreover, recent works proved that metal AM in construction can be a valid technology to reduce CO<sub>2</sub> emissions and increase the efficiency in using high-demand resources [3, 4]. In this sense, among different metal AM processes, WAAM has proved to be the most suitable for efficient structural systems with a reduced environmental impact [5].

Recent applications of WAAM for large-scale structures exploited two different deposition strategies: (i) a “continuous” strategy, i.e., layer-by-layer deposition, suitable for planar and shell elements [6–8] and (ii) a “dot-by-dot” strategy to realize lattice and diagrid structures, such as the awarded WAAM diagrid column designed by the research group at University of Bologna (see, e.g., [9]). Specific considerations must be made when dealing with WAAM elements: (i) the inherent surface roughness, which could influence the mechanical properties [10–14], (ii) the marked mechanical anisotropy due to the specific microstructure [15–21], (iii)

✉ Vittoria Laghi  
vittoria.laghi2@unibo.it

<sup>1</sup> Department of Civil, Chemical, Environmental and Materials Engineering (DICAM), University of Bologna, Bologna, Italy

<sup>2</sup> Department of Industrial Engineering (DIN), University of Bologna, Bologna, Italy

<sup>3</sup> AITIP Centro Tecnológico, Zaragoza, Spain

the influence of process parameters in both geometrical and mechanical response [22–24]. Hence, specific knowledge in advanced manufacturing technology should be combined with structural design competences to efficiently fabricate high-performance WAAM elements [25].

Additively manufactured components, as WAAM plates, are built by the subsequent deposition of layers of molten feedstock material. Evidence of both deposited layers and deposition strategy can be found by analyzing the microstructure. Deposited layers experience a complex thermal cycle, very similar to the case of multi-pass welding; therefore, inhomogeneity and defects in the microstructure can be found [26, 27]. In addition, due to the additive process, some degree of anisotropy in the final parts can be expected, and mechanical properties can vary with regard to the building direction. So far, significant effort has been devoted to the mechanical and microstructural characterization of wall and thin plates produced by WAAM with an ER 70S-6 wire. In literature, tensile properties have been assessed along the building direction (vertical direction) [28] or by comparing vertical and horizontal (parallel to the building plate) directions [24, 29–32]. In few cases, also other extraction directions (i.e., 30°, 45° and 60° to the building plate) were considered [13, 33]. Generally, isotropy in ultimate and yield strengths was found. Also, impact toughness, evaluated for samples extracted from the vertical and horizontal directions, showed no substantial difference in the adsorbed energy [34], thus supporting the isotropic mechanical behavior of ER 70S-6 WAAM thin walls. Fewer works reported anisotropy in ductility, like Rafieazad et al. [32] and Nemani et al. [29], with vertical samples characterized by a lower elongation to failure than horizontal ones. As in vertical samples deposited layers are perpendicularly oriented to the loading direction, the reason for the lower ductility along the building direction was found in: (i) the presence of microstructural defects, such as porosities and lack of fusion, in correspondence of melt pool boundaries that act as stress concentration sites; (ii) formation of brittle phases, such as martensite-austenite in the inter-critical heat-affected zone adjacent to the melt pool; and (iii) grain coarsening in the heat-affected zone.

In the above-mentioned literature works, the differences in microstructure and mechanical properties along the thickness of the WAAM plate and the overlapped layers on the plane parallel to the building platform were not expressly characterized. Therefore, the investigation of the effect on microstructure and mechanical properties of overlapped layers on the plane parallel to the building platform was not highlighted. A first attempt of assessing the effect of thickness was performed by Rafieazad et al. [35] by characterizing block components produced by WAAM. They assessed tensile properties and impact toughness of both horizontal (XY plane, parallel to the deposition direction) and vertical

plane (XZ plane, parallel to the building direction). Tensile properties of horizontal and diagonal samples extracted for the XY plane were comparable, while vertical samples extracted from XZ plane showed lower tensile properties and evidenced an anisotropic behavior along the building direction. However, when considering results of impact tests, the influence of sample extraction directions was less evident.

Moderately thick plates (of the order of few centimeters) are commonly required in various industrial applications, including offshore, aerospace and construction sectors. For example, thick tubular members of offshore jacket platforms can be manufactured using various technologies, including hot and cold forming requiring welding and seamless tube productions. For large tubular joints, cast iron solutions are also preferred, requiring steel grades with special through-thickness properties. Jumbo profiles are also typically required to realize mega-frames in high-rise buildings. One very recent application of thick parts in the aerospace sector is represented by the first metal 3D-printed rocket entirely produced in metal directed energy deposition (DED) technology and launched in space by Relativity Space (see e.g. [36]) with a diameter of over 2 m.

The present work aims at providing a comprehensive study from the fabrication to the characterization of WAAM steel thick plates. Section 2 reports the experimental method adopted to fabricate the samples and characterize them in terms of chemical composition, microstructural features, and mechanical response. The main experimental results are then presented and discussed in Section 3. Finally, the main conclusions are drawn.

## 2 Experimental methods

A wide experimental investigation was carried out to characterize the microstructural and mechanical features of WAAM-produced steel thick plates. The specimens were extracted from two 24-mm thick plates (Fig. 1b, c) along three different directions with respect to the deposition layers and four different relative positions along the thickness.

### 2.1 Material and process

The plates were produced at AITIIP Centro Tecnológico (Spain). The adopted welding machine was a Fronius TPS 500i with Fronius WF 60i ROBACTA DRIVE CMT welding torch and a SplitBox SB 60i R as buffer. The welding torch was mounted on a Comau NJ-130 robot (Fig. 1a). The set of printing parameters was assessed from an autonomous working cell Kraken (as outcome of MEGAROB Project, see, e.g., [37]). The wire feed used was a 1.2-mm Lincoln Electric UltraMag (ER 70S-6). The welding gas used was SanArc8, a mixture of Ar and CO<sub>2</sub>.



(a)



(b)



(c)

**Fig. 1** Fabrication of the tested plates: (a) robotic set-up, (b) detail on the plate thickness, (c) full plate

The following process parameters were adopted to fabricate the plates: wire feed rate of 7.5 m/min, 2.25-mm layer height, robot printing velocity (during printing) of

0.018 m/s, robot travel velocity (between printing) of 0.06 m/s, 238 A current and 16.34 V voltage, with 15 l/min gas flow rate.

The initial printing parameters based on the work by Nagasai et al. [38] were fine-tuned to the specific characteristics of the AITIIP printing set-up. The robot speed was adjusted to reduce the thickness of the single layer, thus substantially improving the geometrical quality, while reducing the thermal transfer. The optimal compromise between thickness of single layers and geometrical precision was found using a printing velocity of 0.018 m/s leading to a nominal layer thickness of 3–5 mm.

As shown in Fig. 1b, the deposition strategy to realize each layer consisted in a continuous deposition for the two perimeter layers, or contour, of nominal thickness in the range of 3–5 mm and a zig-zag pattern to fill the layer volume, which was rotated every single layer by 30°, in order to obtain the total nominal wall thickness of 24 mm (Fig. 1c). Beads of molten material were deposited with a 3.5-mm distance, and dwell time was set as a function of the part temperature, which was kept under 250 °C for the whole process.

## 2.2 Sample fabrication

Once fabricated, the two plates were machined to eliminate the superficial oxidation and reduce surface roughness, obtaining a final thickness of roughly 19 mm. Then, different types of machined specimens were extracted (Fig. 2). First, to characterize the plate along the three main planes ( $XY$ ,  $XZ$ , and  $YZ$  as defined in Fig. 2b), bulk parallelepiped samples ( $30 \times 30 \times 19 \text{ mm}^3$ ) were extracted from the area indicated by red squares in Fig. 2b, preserving the whole plate thickness. These samples were utilized for microstructural analyses and to verify the elastic modulus via non-destructive ultrasonic method [39].

Additionally, a series of samples for mechanical characterization were extracted with the aid of wire electrical discharge machining (wire-EDM). Different orientations were considered with respect to the deposition layers, i.e., parallel to the deposition layer ( $L$ ), perpendicular to it ( $T$ ), and at 45° ( $D$ ), and at different positions along the thickness, identified as level 1, level 2, level 3, and level 4 in Fig. 2b. In detail, a total number of 24 dog-bone shaped tensile specimens were extracted having 4-mm nominal thickness and straight length of 270 mm at 3 different orientations and 4 different levels of thickness, with 2 repetitions for each type. At the same orientations, a total of 30 flat parallelepiped specimens, having nominal thickness of 2.5 mm and straight length of 55 mm, were obtained for the impact tests.



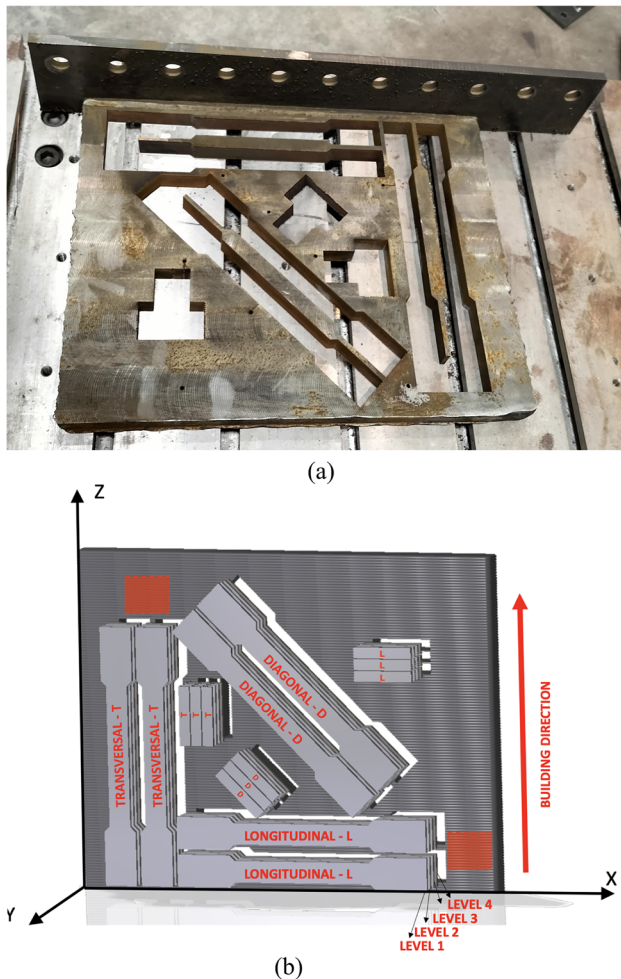


**Fig. 2** Fabrication of the samples: (a) extraction of the samples; (b) graphical representation of the sample extraction with respect to the printing orientation and level with respect to the plate thickness

### 2.3 Chemical composition and microstructural characterization

Chemical composition of the WAAM plates was evaluated with glow discharge optical emission spectroscopy (GDOES, 4-mm diameter sputtered burnt spot). Microstructure of WAAM plates was characterized along the whole plate thickness on  $XY$ ,  $XZ$ , and  $YZ$  planes (Fig. 2) by cutting metallographic samples from bulk parallelepiped samples. Prior to microstructural characterization, samples were subjected to a standard metallographic preparation up to mirror polishing with 1- $\mu\text{m}$  diamond suspension and chemical etching with Nital 2% [40]. Microstructural features were investigated with both optical (OM) and field-emission gun scanning electron microscopy equipped with an energy-dispersive X-ray spectroscope for localized elemental analyses (FEG-SEM EDS).

### 2.4 Mechanical characterization

The tensile tests were carried out on dog-bone specimens having dimensions defined according to ISO 6892–1 standard test protocol [41]. The ID of each specimen is defined as follows: (i) specimen location along thickness (i.e., 1, 2, 3, 4), (ii) specimen orientation (i.e.,  $L$ ,  $D$ ,  $T$ ), and (iii) specimen number (i.e., 1, 2). As an example, the specimen ID 1L-1 indicates the first specimen oriented along the longitudinal direction and located at level 1 along the thickness.

The tensile tests were carried out using a universal hydraulic machine (Fig. 3a). The tests were conducted in displacement control until failure, with a varying velocity between 0.3 and 0.5 mm/min (lower until yielding, then increasing until failure) following the ISO 6892–1 standard test protocol specifications [41].

The axial elongations were recorded using a 100-mm extensometer, and average longitudinal strains were calculated to obtain the stress–strain curves. The tangent Young’s modulus values were calculated from the stress–strain curves through an ordinary least squares regression (OLSR) to identify the average longitudinal Young’s modulus  $E$  according to the method proposed by [10] and adopted also in [13, 20].

Additionally, a total of 8 specimens (2 longitudinal, 3 transversal, and 3 diagonal, taken at different levels of thickness) were monitored with digital image correlation (DIC) as well, an image-based monitoring system able to capture the full field of strain during the entire test (Fig. 3b,c). Prior to testing, the front of the specimens monitored under DIC was sprayed with white matt paint, while a random pattern of black speckles was subsequently applied (see Fig. 3c for reference of typical tested coupons monitored with and without DIC). The DIC system was employed to provide complementary data allowing to reconstruct the full surface strain field along the entire gauge length. This accurate surface strain field allows to compute both the longitudinal (i.e., along longitudinal direction of the specimen) and transversal (i.e., along the transversal direction of the specimen) strains. The analysis of the captured strain field makes possible to detect non-uniform strain field under macroscopic uniaxial loading, which is typical of not-machined WAAM pieces (see, e.g., [10, 13, 20, 42]). The outputs of the DIC were processed using Vic3D software to obtain both the longitudinal and transversal surface strain fields (punctual values). The detailed analysis and discussion of the strain fields obtained from the DIC data is out of the scope of the present paper and will be presented in future work.

The average longitudinal and transversal strains were evaluated from the DIC data by means of virtual extensometers to compute the values of the Poisson’s coefficient (ratios between the average transversal and longitudinal strains, see Fig. 3d). The OLSR method was additionally used to evaluate the average values of Poisson’s ratios.

**Fig. 3** (a) Tensile test set-up; (b) DIC monitoring; (c) post-failure specimens monitored with (left-hand side) and without (right-hand side) DIC system; (d) average longitudinal and transversal strains as obtained from DIC

Impact tests were performed with a Charpy pendulum (300 J capacity) on V-notch sub-sized samples ( $55 \times 10 \times 2.5 \text{ mm}^3$ ) according to the specifications given by EN ISO 148–1:2016 [43]. The specimens taken were taken from the flat parallelepiped specimens extracted from plates. Five samples for each extraction direction ( $T, L, D$ ) taken along the plate thickness have been tested at both room temperature (approx.  $20 \text{ }^\circ\text{C}$ ) and low temperature ( $-20 \text{ }^\circ\text{C}$ ), for a total of 30 samples.

Fracture surfaces of both tensile and impact tests specimens were observed at high magnification by FEG-SEM to investigate failure mechanisms.

### 3 Results and discussion

#### 3.1 Compositional analysis

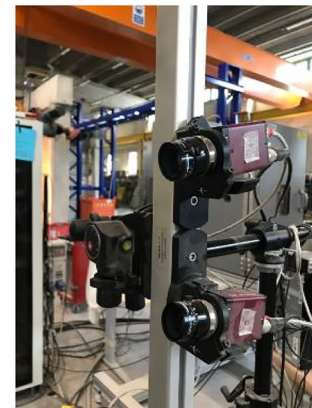
The chemical composition of the WAAM plate, reported in Table 1, complies with the specification given by EN 10025–2 [44] for non-alloy structural steels. In fact, the ER 70S-6 wire, whose nominal composition is reported in the same table for reference, is one of the most used filler wires for arc welding of generic structural steels such as S185, S235, S275, and S355. Considering products of comparable thickness, according to the EN 10025–2, these steels should contain a maximum of 0.27 wt.% of C, 1.8 wt.% of Mn, 0.6 wt.% of Si, and 0.045% of both P and S. The WAAM plate, as anticipated, complies with the specifics. The slightly higher amount of Si in the WAAM plate is due to the feedstock material, as Si is often added to filler wires as deoxidizer and to improve fluidity. It is also worth noticing the extremely low amount of C, especially relevant if correlated to the good overall mechanical properties discussed in the following sections, which are comparable to regular S275 steel.

#### 3.2 Microstructural characterization

Microstructural analyses, carried out on bulk parallelepiped samples ( $30 \times 30 \times 19 \text{ mm}^3$ ) extracted from machined plates, revealed a generally sound microstructure with minor traces of typical solidification defects (i.e., gas porosities) as evidenced by micrographs in Figs. 4 and 5. As expected from the chemical composition results in Table 1, a ferritic microstructure with a low-volume fraction of perlite was found. WAAM, like other additive processes, results in a distinctive microstructure and, even if microstructural analyses



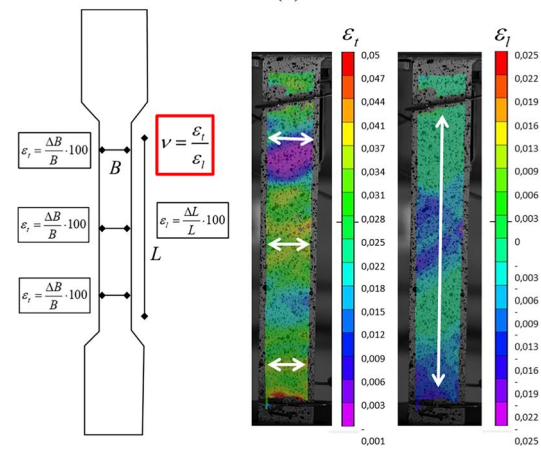
(a)



(b)



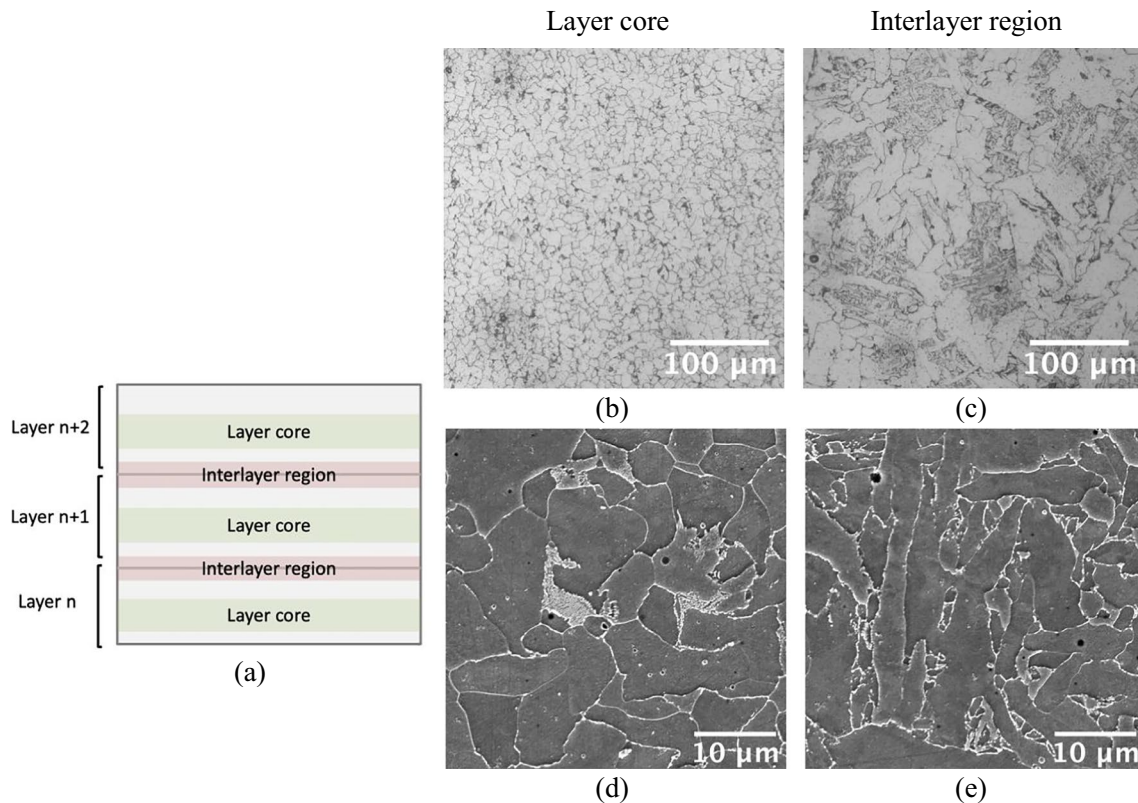
(c)



(d)

**Table 1** Chemical composition of the WAAM plate, evaluated by GDOES, compared to the nominal composition of the ER 70S-6 feedstock wire [45]

	Element (wt.%)						
	Fe	C	Mn	Si	P	S	Other
ER 70S-6 Wire	Bal	0.078	1.4	0.85	–	–	–
WAAM Plate	97.499 ± 0.015	0.071 ± 0.001	1.338 ± 0.002	0.776 ± 0.011	0.024 ± 0.001	0.014 ± 0.0004	0.278

**Fig. 4** Optical and scanning electron microscopy of the XZ plane of the WAAM plate showing: (b, d) the microstructure in correspondence of layers core consisting of fine polygonal ferrite with perlitic islands; (c, e) the microstructure in correspondence of interlayer

regions consisting of different ferritic morphologies, including polygonal and acicular ferrite. Schematic representation of the regions is given in (a)

revealed an essentially homogeneous microstructure along the three main planes, traces of the subsequent deposited layers can be recognized. According to the deposition process and the contouring strategy applied for each layer, traces of the deposited layers can be easily detected on the XZ plane. In particular, two distinct regions can be clearly identified, as schematized in Fig. 4a: (i) the layer core, where the microstructure is to a lesser extent affected by the subsequent thermal cycles and is typically characterized by the finest microstructure; (ii) an interlayer region, located near layer boundaries, where the microstructure is affected by complex heating cycles due to the subsequent deposition of molten material. Ferrite morphology varied within WAAM plates depending on the location within the deposited

layer, as shown in Fig. 4b–e and as also observed by other authors [24, 32, 35]. In the layer core, a homogeneous and fine microstructure mainly consisting of polygonal, or equiaxed, ferrite with small perlite islands was found (Fig. 4b). Perlite islands were better resolved at FEG-SEM analyses (Fig. 4d), which revealed the typical plate-like lamellar morphology of alternating ferrite and cementite plates. In the interlayer regions, along with the polygonal ferrite, also other ferrite morphologies could be observed (Fig. 4c and e), as also reported by [32, 35]. This region is more affected than layer core by solid-state transformations occurring in non-equilibrium conditions during the subsequent deposition of layers. Like in a multipass welding process, due to the heating induced by the deposition of molten material, the



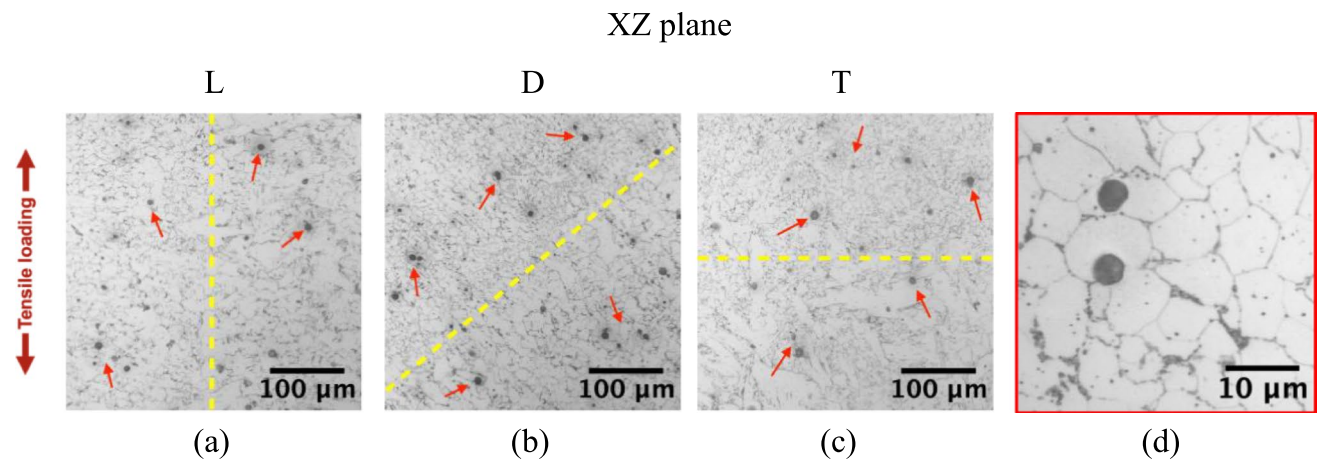


**Fig. 5** Optical micrographs showing interlayer region in samples for mechanical tests: (a) longitudinal, (b) diagonal and (c) transverse sample. In the micrographs, yellow dashed lines schematize layers

orientation according to tensile loading direction, and red arrows highlight some gas porosities. In (d), a detail of representative gas porosities

previously solidified metal re-austenitized and, during rapid cooling, austenite to ferrite transformations occur. Austenite decomposes first in allotriomorphic ferrite, then in Widmanstatten ferrite and eventually in acicular ferrite, which nucleates from inclusions [46–49]. Acicular ferrite is often identified as a “basket-weave structure” and, in weldments of low and mild steels, can easily co-exist with allotriomorphic, polygonal, and Widmanstatten ferrite [47, 48]. The

presence of non-metallic inclusions promotes the formation of acicular ferrite at the expenses of bainite. As will be better explained later in the text when discussing fractographic analyses, a widespread dispersion of non-metallic inclusions rich in Si, S, and Mn was found, which can justify the evolution into acicular ferrite upon cooling. Acicular ferrite is known to improve strength and especially toughness of the

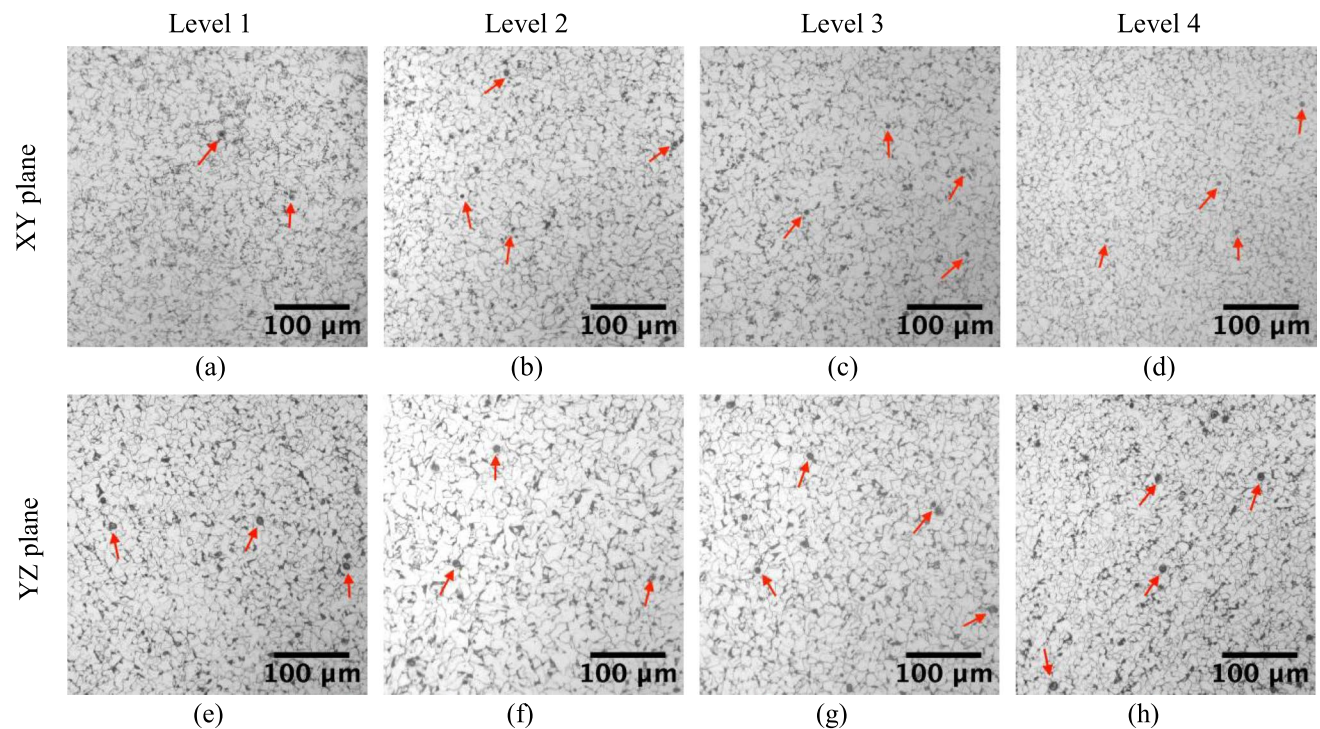
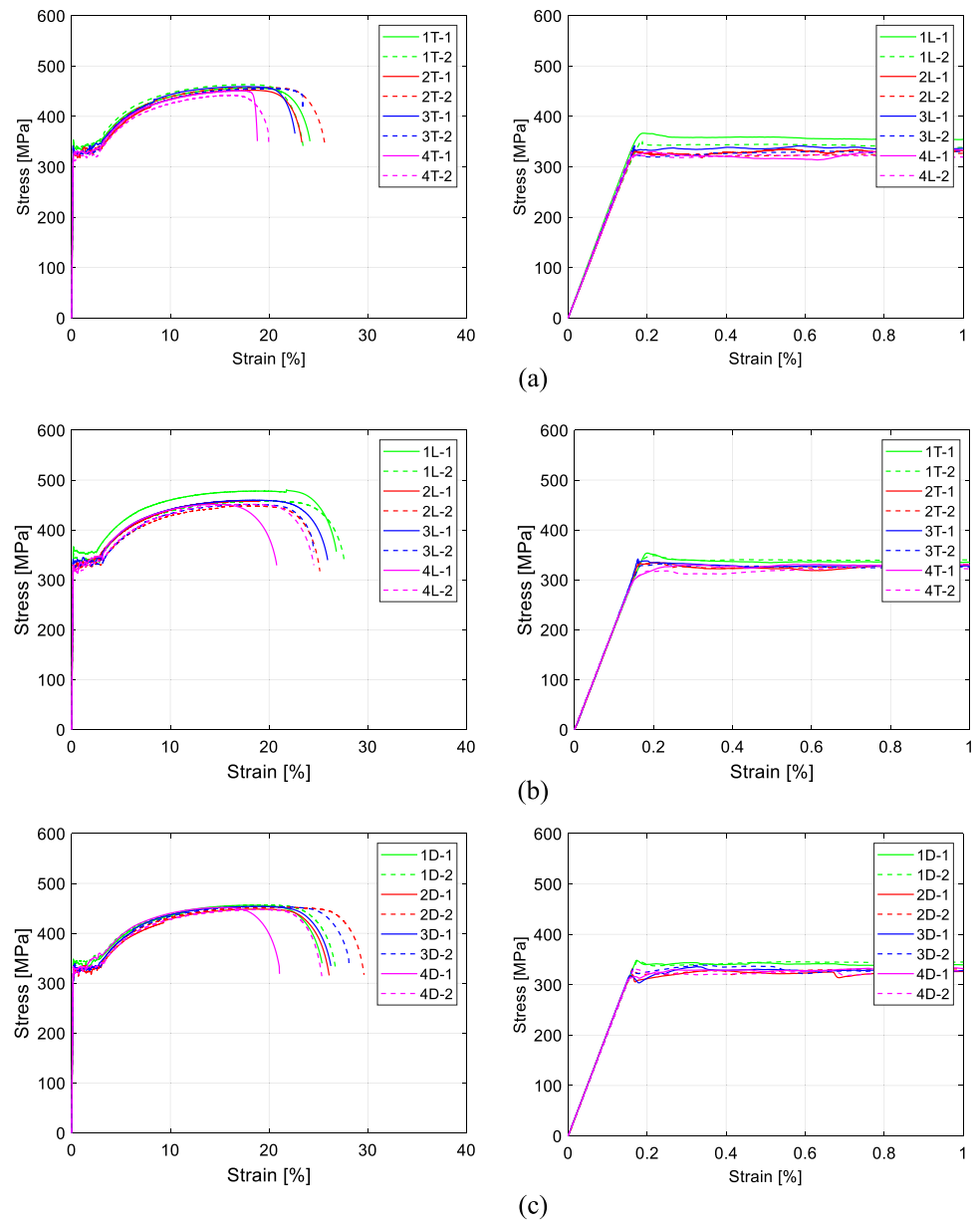


**Fig. 6** Optical microscopy of the XY and YZ plane showing the evolution of the microstructure along the thickness of the WAAM plate: (a, e) level 1, (b, f) level 2, (c, g) level 3, (d, h) level 4. Red arrows highlight some gas porosities

**Fig. 7** Stress–strain whole curves (on the left) and zoom for strain lower than 1% (on the right) for (a) *T* specimens, (b) *L* specimens, (c) *D* specimens



alloy [46–49]; therefore, its presence in correspondence of interlayer region it is not undesired.

By referring to the extraction directions of specimens for mechanical tests (L, D, T), the orientation of the interlayer regions changes with reference to the loading direction, as displayed in Fig. 5: (i) *T* specimens have layers parallel to the base platform and perpendicularly oriented to the loading direction; (ii) *L* specimens are characterized by layers oriented along the loading direction; (iii) *D* specimens present a 45° tilt angle between layers and loading direction. However, as will be discussed in the following section, the different layer orientation in *L*, *T*, and *D* specimens did not significantly affect the mechanical behavior. The reason can

be found in the beneficial presence of acicular ferrite in the interlayer region, but more importantly in the complex deposition strategy adopted to deposit each layer that promoted microstructural homogeneity between different planes and loading directions (Figs. 5 and 6). Microstructural fineness in both layer core and interlayer region and a gradual transition from the core of the layer to the interlayer region were also promoted by the deposition strategy, as it can be seen in Fig. 5. These aspects improved the isotropic mechanical response of the material, as it will be later explained. The deposition strategy also reduced the presence of large defects, especially in the interlayer region, further supporting the good overall mechanical behavior. In fact, as shown



**Table 2** Summary of the average key mechanical parameters from tensile tests

Specimen		$E$ (GPa)	$f_y$ (MPa)	$\epsilon_y$ (%)	$f_u$ (MPa)	$\epsilon_u$ (%)	$\epsilon_r$ (%)	$\mu$ (-)
L	1	206	350	0.17	469	21	27	160
	2	201	330	0.16	454	18	25	157
	3	204	337	0.17	455	18	25	153
	4	204	317	0.16	452	16	23	146
	<b>Mean</b>	<b>204</b>	<b>333</b>	<b>0.16</b>	<b>457</b>	<b>18</b>	<b>25</b>	<b>154</b>
	<b>COV</b>	<b>2.1%</b>	<b>4%</b>	<b>4%</b>	<b>2%</b>	<b>11%</b>	<b>9%</b>	<b>7%</b>
	T	1	204	346	0.17	460	18	24
2		205	328	0.16	455	18	24	153
3		205	326	0.16	457	19	23	145
4		204	327	0.16	446	17	19	121
<b>Mean</b>		<b>205</b>	<b>332</b>	<b>0.16</b>	<b>455</b>	<b>18</b>	<b>23</b>	<b>140</b>
<b>COV</b>		<b>0.8%</b>	<b>3%</b>	<b>3%</b>	<b>1%</b>	<b>7%</b>	<b>10%</b>	<b>9%</b>
D		1	205	348	0.17	456	19	26
	2	206	327	0.16	450	19	28	175
	3	205	336	0.16	454	19	27	166
	4	204	327	0.16	450	17	23	145
	<b>Mean</b>	<b>205</b>	<b>335</b>	<b>0.16</b>	<b>453</b>	<b>19</b>	<b>26</b>	<b>160</b>
	<b>COV</b>	<b>0.9%</b>	<b>3%</b>	<b>3%</b>	<b>0.7%</b>	<b>8%</b>	<b>10%</b>	<b>10%</b>

in Fig. 5a, b and c with a detail given in Fig. 5d, porosities spherical in shape with size of tens of micrometers were homogeneously distributed along the whole microstructure.

Further supports to these findings can be found by analyzing the microstructure along plate thickness on  $XY$  and  $YZ$  planes, as reported in Fig. 6. The figure compares the microstructure observed near plate edges (i.e., levels 1 and 4) and in plate center (i.e., levels 2 and 3) of different planes (parallel and orthogonal) to the building direction. Analyses revealed a homogeneous microstructure also along the plate thickness where polygonal, or equiaxed, ferrite with perlite colonies is the predominant microstructure. Plate edge and center differ substantially for the dimension of the ferritic grain, being slightly coarser in correspondence of the plate center (levels 2 and 3). However, microscopic analyses identified no major discontinuities along the plate thickness and a homogeneous dispersion of small spherical porosities (some of them indicated by red arrows in Fig. 6) in the microstructure.

### 3.3 Tensile tests

Figure 7 shows the engineering stress strain curves as obtained from the tensile tests on dog-bone specimens

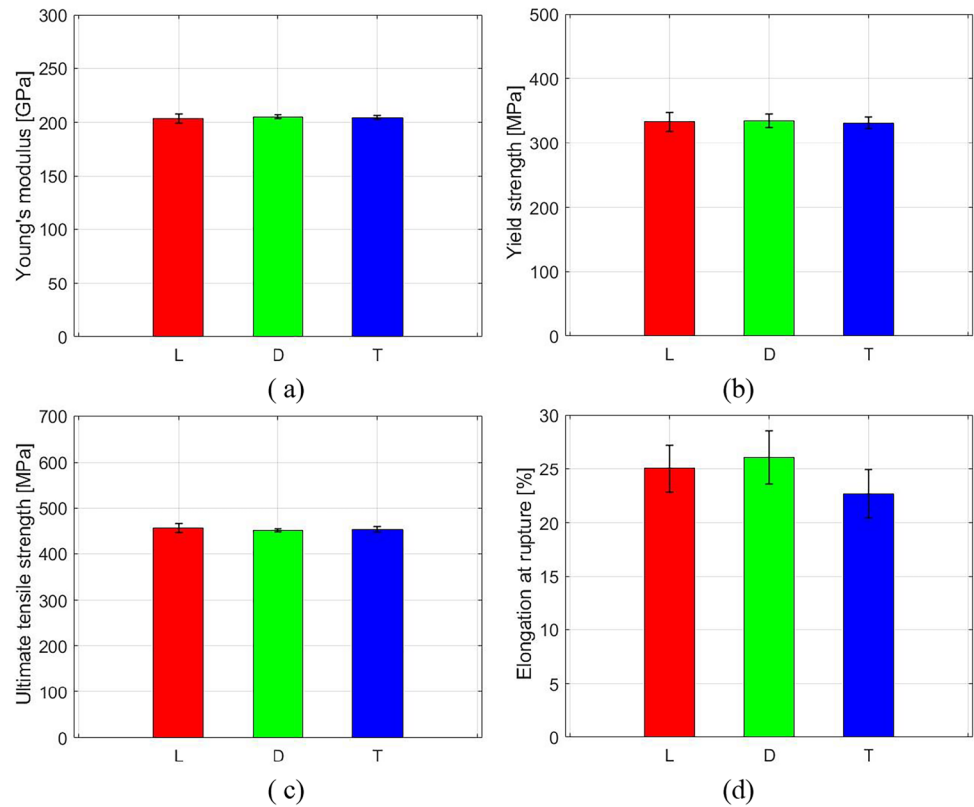
including both the full strain range (on the left) and a zoom of it to (on the right) a strain limit of 1%. The curves are typical of hot-rolled steels with a first linear elastic behavior followed by a pseudo-horizontal yielding plateau identifying the yielding region and ending with a final strain hardening region up to failure. The following key mechanical parameters were determined from the stress–strain curves, including longitudinal Young’s modulus  $E$ , Poisson’s ratios  $\nu$ , yield strength  $f_y$ , ultimate strength  $f_u$ , yield strain  $\epsilon_y = f_y/E$ , elongation at ultimate strength  $\epsilon_u$ , elongation at rupture  $\epsilon_r$  and strain ductility  $\mu = \epsilon_r/\epsilon_y$ .

In most cases, the yielding point was very well defined, while in only few cases a somewhat rounded shape was observed, similar to the curves reported in [13]. The comparison of the full stress–strain curves of the different types of specimens does not show a clear influence of the specimen orientation and location along the thickness in the tensile response. The zoom at small strains reveals, for some specimens, a slightly rounded curve with a not well-defined yielding point. This motivated the choice of the 0.2% proof strength as measure of the yield strength, following the same approach as reported in [13].

**Table 3** Ratios of key mechanical parameters with respect to the specimens orientation

Ratio	$E$ (-)	$f_y$ (-)	$\epsilon_y$ (%)	$f_u$ (-)	$\epsilon_u$ (-)	$\epsilon_r$ (-)	$\mu$ (-)
$L/T$	1.00	1.01	1.01	1.01	1.02	1.10	1.10
$L/D$	0.99	1.00	1.00	1.01	0.98	0.96	0.96
$D/T$	1.00	1.01	1.01	1.00	1.04	1.15	1.14
$D/L$	1.01	1.00	1.00	0.99	1.02	1.04	1.04

**Fig. 8** Bar charts providing the average values of the key mechanical parameters highlighting the influence of specimen orientation and position along the thickness: **(a)** Young's modulus; **(b)** yield strength; **(c)** ultimate tensile strength; **(d)** elongation at rupture



The measured values of Young's moduli (ranging between 200 and 210 GPa) and Poisson's ratios (ranging between 0.26 and 0.4) are within the typical ranges of conventional normal-strength carbon steels [50]. This result was also confirmed by ultrasonic analyses that by measuring the elastic constants on  $XY$ ,  $XZ$ , and  $YZ$  planes. The analyses revealed a substantial isotropy in the elastic behavior with  $E = 211 \pm 1$  GPa ( $XZ$  plane),  $214 \pm 1$  GPa ( $XY$  plane), and  $214 \pm 2$  GPa ( $YZ$  plane).

The measured values of yield strength (ranging between 315 and 360 MPa), ultimate tensile strength (ranging between 440 and 480 MPa), and elongation at rupture (ranging between 19 and 28%) are in general lower than the values stated by the manufacturer for conventional welds [45], but adequate for structural applications. In fact, by comparing tensile results to the specification given by EN 10025-2 [44] for non-alloy structural steels, ER 70S-6 WAAM plates comply with the conventional S275 J2 steel, also considering the impact toughness values discussed in Sect. 3.4. In addition, all curves evidence strain hardening ratios value  $f_u/f_y > 1.10$ , therefore satisfying the requirements given by EC3 [50] for normal-strength structural steel, and good ductile behavior with values of elongation at rupture typically within 20–30%. Only few transversal specimens evidenced a slightly lower ductility with values of elongation at rupture between 18 and 20%. In any case, all specimens satisfied the

requirement of  $\epsilon_r > 15\%$  for normal-strength structural steel provided by EC3 [50].

Tables 2 and 3 and the bar charts of Fig. 8 provide a summary of the key mechanical parameters along the different thickness levels and directions to highlight the potential influence of the specimen orientation and position along the thickness on the tensile behavior.

Table 2 provides the average values of selected key mechanical parameters for each level (1, 2, 3, 4) along the thickness and for each orientation ( $L$ ,  $T$ ,  $D$ ). The average

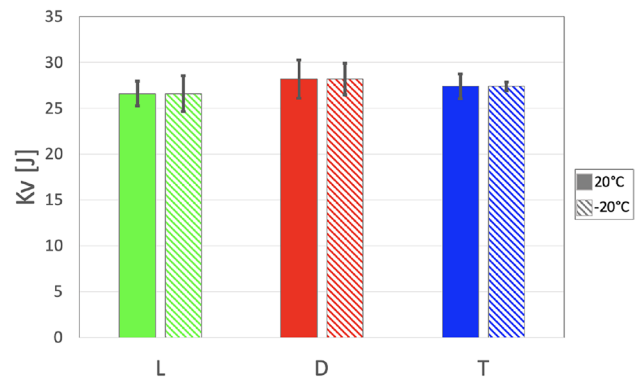


**Fig. 9** Results of impact tests (average and standard deviations) performed at 20 °C and -20 °C for  $L$ ,  $D$ , and  $T$  orientations along the plate thickness

**Table 4** Normalized impact toughness evaluated from tests performed on sub-sized specimens (average values)

Direction	Kv [J]			
	20 °C		−20 °C	
	Sub-sized specimens	Normalized	Sub-sized specimens	Normalized
L	27	108	27	108
D	28	112	28	112
T	27	108	27	108

is computed considering the two tested specimens of the same type. The mean values do not show a significant variation across the thickness and do not evidence any systematic trend, apart from a very slight increase of some properties for level 1 along the longitudinal direction *L*. All key mechanical parameters show small variabilities along the thickness, with minimum COV values (less than 1%) observed for Young's modulus. Yield and ultimate strengths, as well as yield strains, exhibit COV values around 0.7–4%. Higher through-thickness variability is observed for values of elongation at ultimate strength and elongation at rupture, showing maximum COV of 11%. In addition, Table 2 provides, for each orientation, mean values and coefficient of variation (COV) considering the 8 specimens over the four levels oriented along the same direction. For the sake of clearness, mean values and standard deviations are also represented in the bar charts of Fig. 8. All mean values exhibit

little variation along the 3 directions, which are further quantified in terms of ratios as reported in Table 3. On average, Young's modulus values are almost constant along the three directions (ratios between 0.99 and 1.01), thus indicating an almost perfectly isotropic elastic behavior. The smallest/highest values of the ratios are, instead, observed for the elongation at rupture and ductility (with minimum/maximum ratios between 0.95 and 1.15). The other key mechanical parameters exhibit ratios between 0.98 and 1.04. Overall, the obtained results indicate a very mild anisotropy, thus in line with previous results obtained on WAAM carbon steels [21, 51].

### 3.4 Impact tests

Impact toughness of sub-sized samples extracted from WAAM plates ranged between 27 and 28 J. As showed by the bar chart in Fig. 9, no significant difference was evidenced among sample extraction direction (*L*, *D*, *T*) or along plate thickness. In fact, standard deviations, which represent the variability along the thickness, are rather reduced. As an interesting result, the impact toughness was maintained even when tested at low temperature (−20 °C). It is worth noticing that none of the tested samples reached the complete break, thus suggesting a significant level of ductility. Fractographic analyses, discussed in the following section, demonstrated that fracture was fully ductile; thus, 100% shear fracture according to ASTM E23-18 [52]. Therefore, following the work of

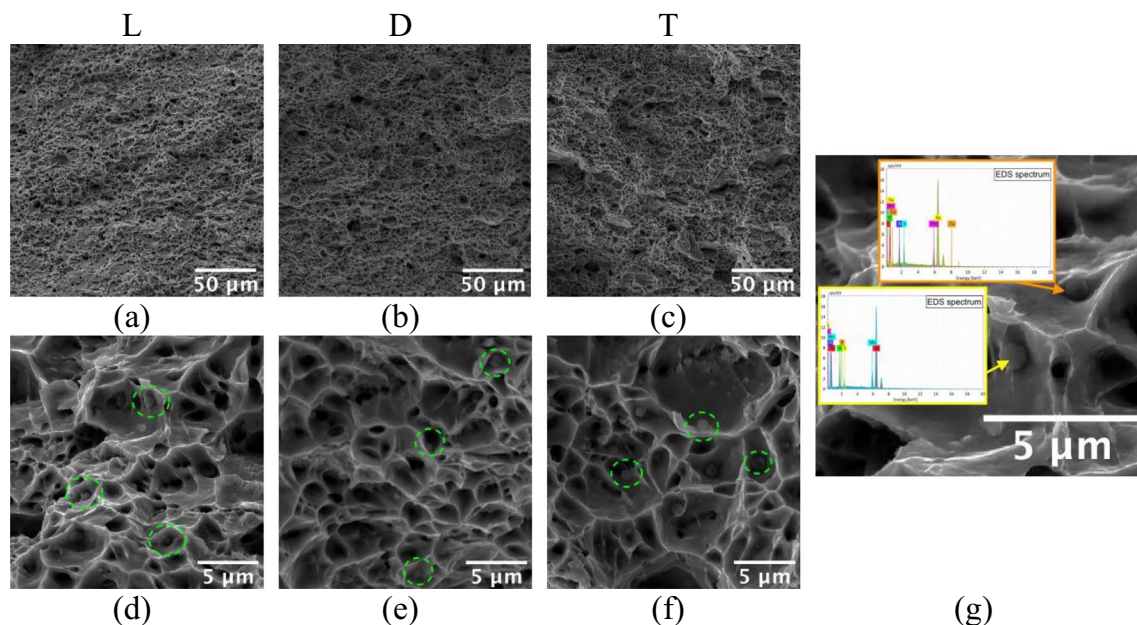
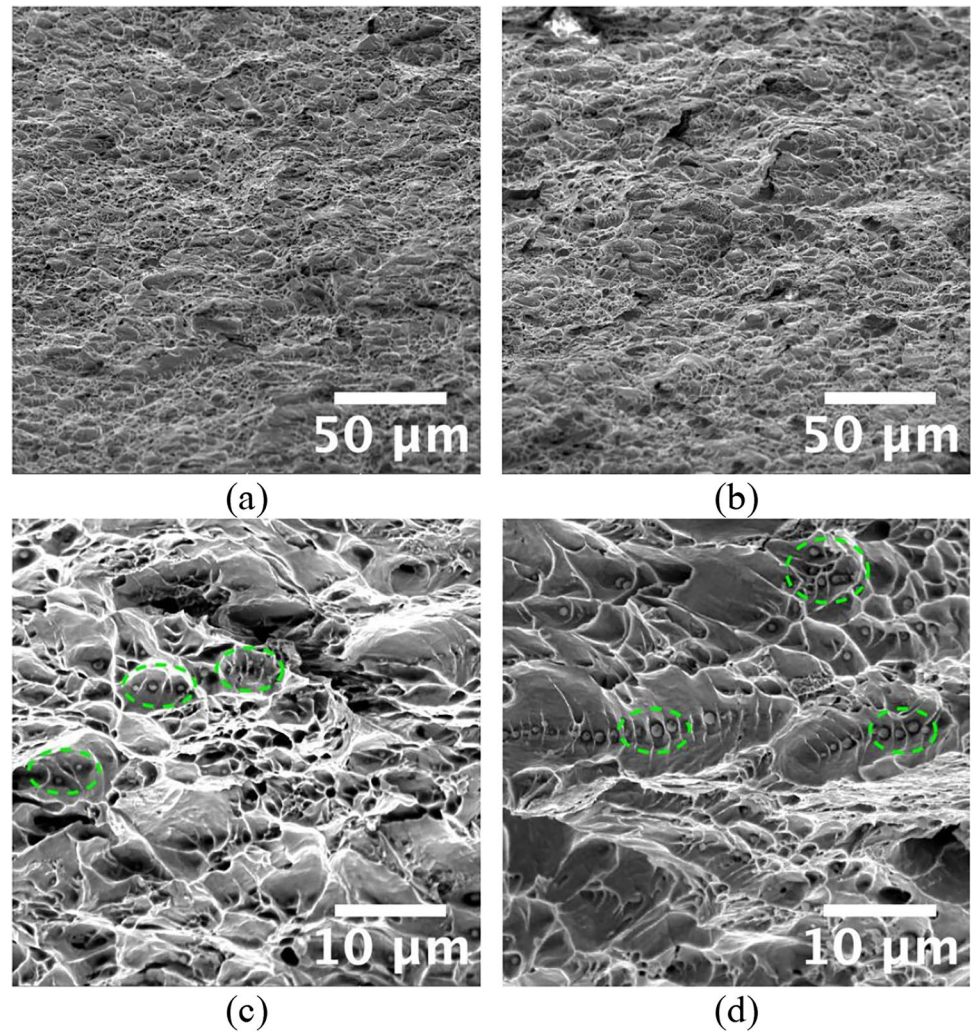


**Fig. 10** Representative fracture surfaces of tensile samples observed by FEG-SEM at low and high magnification: (a, d) longitudinal; (b, e) diagonal; (c, f) transversal samples. Green dashed circles highlight

some of the non-metallic inclusions found on fracture surfaces. In (g), representative semi-quantitative analyses showing enrichment of Mn, Si, and S in correspondence of inclusions



**Fig. 11** Representative fracture surfaces of impact test samples observed by FEG-SEM at low and high magnification on longitudinal orientation tested at: (a, c) 20 °C; (b, d) –20 °C. Green dashed circles highlight some of the non-metallic inclusions found on fracture surfaces



Lucon, McCowan, and Santoyo [53] already applied to ER 70S-6 WAAM sub-sized specimen by Waqas et al. [34, 54], also the normalized impact toughness was calculated from the sub-sized adsorbed energy resulting from the tests. Results are reported in Table 4.

### 3.5 Fracture surfaces

Fracture surfaces of both tensile (Fig. 10) and impact test (Fig. 11) samples were investigated at high magnification by FEG-SEM to investigate fracture mechanisms. Representative fracture surfaces of tensile samples are reported in Fig. 10, showing a ductile morphology characterized by typical microvoids, termed dimples, nucleated and growth in correspondence of non-metallic inclusions. The inclusions are clearly visible in high magnification analyses in Fig. 10 (d–f) as sub-micrometric spherical particles. Localized EDS analyses (Fig. 10(g)) showed an enrichment of Si, S, and Mn in correspondence of the particles, suggesting type I MnS inclusions.

The lack of scan track marks or preferential fracture directions on the fracture surface supports the isotropic mechanical response of the material promoted by the above-discussed homogeneous microstructure, achieved by the complex deposition strategy and partial remelting of the previously solidified layers. Furthermore, no substantial differences were observed on the fracture surfaces of the samples, regardless of the direction of extraction or the position along the plate thickness, supporting the isotropic mechanical behavior resulting from the mechanical tests.

The same inclusions observed on tensile samples were also found on fracture surfaces of impact test samples, as demonstrated by micrographs reported in Fig. 11, mainly when observed at high magnification (Fig. 11c, d). As a representative example, fracture surfaces at both 20 °C and –20 °C for the *L* orientation are reported in the figure. As discussed in the previous section, a fully ductile fracture was evidenced by very fine dimples for all tested samples without evidence of different fracture mechanisms among the analyzed extraction/load direction conditions,

supporting the isotropic mechanical behavior evidenced by test results. Results also showed that ductile behavior was preserved even when tested at low temperatures, and, as a confirmation, an analogous morphology was found on samples tested at 20 °C (Fig. 11a, c) and at –20 °C (Fig. 11b, d).

## 4 Conclusions

Metal additive manufacturing, and in particular wire-and-arc additive manufacturing (WAAM), has proven to be a very efficient solution to realize new structural elements and metallic parts for various industrial applications, including construction industry. However, most of the research effort has been dedicated to thin shell (single layers) structures, and specific experimental studies are needed to provide insights into the possible influence of higher thickness (multiple layers) in the mechanical behavior of large parts.

The present study reported an extensive experimental investigation from the microstructural and mechanical points of view of WAAM-produced thick walls with ER70S-6 wire.

Microstructural analyses revealed a fine ferritic microstructure with a low volume fraction of perlitic islands, as also confirmed by compositional analyses that showed an extremely low amount of C (0.071 wt.%). Along the plate thickness, microstructure was found as homogeneous and mainly consisting of fine polygonal ferrite.

From the mechanical tests on specimens taken at different levels of thickness and different orientations, the following considerations can be made. In general, results provided values of the key mechanical parameters (Young's modulus, yield strength, ultimate tensile strength and impact toughness) adequate for structural applications, according to the recommendations from the Eurocode provisions, with strength values in line with S275 structural steel. Levels of ductility are quite higher than the minimum recommended values for structural steel. Both aspects can be explained by the very fine microstructure and the absence of large microstructural defects. Results also showed very little differences on the key mechanical parameters from specimens taken at different orientations and different location along the thickness, thus proving an overall isotropic mechanical behavior. This result is well supported by microstructural as well as fractographic analyses that revealed a substantially homogeneous microstructure along the whole plate.

Hence, WAAM-produced thick walls resulted to be good-quality products in terms of their mechanical performances to be implemented in large-scale construction applications. Future studies will be carried out on as-built specimens to assess the influence of surface roughness and other possible geometrical irregularities on the mechanical behavior.

**Author contribution** Conceptualization: VL; validation: VL; investigation: LA, LT, GDE; resources: IM, AL; funding acquisition: JAD, MP; writing — original draft: VL, LA, LT; writing — reviewing and editing: LC, MP; supervision: MP.

**Funding** Open access funding provided by Alma Mater Studiorum - Università di Bologna within the CRUI-CARE Agreement. The research has been funded within the “AGRIAM” project—Call for SMEs within 3DP PAN EU project 2020 (<https://3dppan.eu>), co-funded by the European Parliament and managed by the European Commission. READI (Network of Excellence in Additive Manufacturing) CER-20191020 EXP00122598- CERVERA provided co-funding to AITIIP.

**Data Availability** Data will be available upon request to the corresponding author.

## Declarations

**Competing interests** The authors declare no competing interests.

**Open Access** This article is licensed under a Creative Commons Attribution 4.0 International License, which permits use, sharing, adaptation, distribution and reproduction in any medium or format, as long as you give appropriate credit to the original author(s) and the source, provide a link to the Creative Commons licence, and indicate if changes were made. The images or other third party material in this article are included in the article's Creative Commons licence, unless indicated otherwise in a credit line to the material. If material is not included in the article's Creative Commons licence and your intended use is not permitted by statutory regulation or exceeds the permitted use, you will need to obtain permission directly from the copyright holder. To view a copy of this licence, visit <http://creativecommons.org/licenses/by/4.0/>.

## References

1. Wu P, Wang J, Wang X (2016) A critical review of the use of 3-D printing in the construction industry. *Autom Constr* 68:21–31
2. Boje C, Guerriero A, Kubicki S, Rezgui Y (2020) Towards a semantic construction digital twin: directions for future research. *Autom Constr* 114:103179
3. Kanyilmaz A, Demir AG, Chierici M, Berto F, Gardner L, Kandukuri SY, Kassabian P, Kinoshita T, Laurenti A, Paoletti I, du Plessis A, Razavi SMJ (2022) Role of metal 3D printing to increase quality and resource-efficiency in the construction sector. *Addit Manuf* 50:102541. <https://doi.org/10.1016/J.ADDMA.2021.102541>
4. Sauerwein M, Doubrovski E, Balkenende R, Bakker C (2019) Exploring the potential of additive manufacturing for product design in a circular economy. *J Clean Prod* 226:1138–1149
5. Priarone PC, Pagone E, Martina F, Catalano AR, Settineri L (2020) Multi-criteria environmental and economic impact assessment of wire arc additive manufacturing. *CIRP Ann* 69:37–40
6. Gardner L, Kyvelou P, Herbert G, Buchanan C. Testing and initial verification of the world's first metal 3D printed bridge. *J Constr Steel Res.* 172 (2020). <https://doi.org/10.1016/j.jcsr.2020.106233>.
7. Lange J, Feucht T, Erven M (2020) 3D printing with steel: additive manufacturing for connections and structures. *Steel. Construction* 13:144–153
8. Evans SI, Wang J, Qin J, He Y, Shepherd P, Ding J (2022) A review of WAAM for steel construction – manufacturing, material and geometric properties, design, and future directions. *Structures* 44:1506–1522. <https://doi.org/10.1016/j.istruc.2022.08.084>

9. Laghi V, Palermo M, Gasparini G, Trombetti T. Computational design and manufacturing of a half-scaled 3D-printed stainless steel diagrid column. *Addit Manuf.* 36 (2020). <https://doi.org/10.1016/j.addma.2020.101505>.
10. Kyvelou P, Slack H, DaskalakiMountanou D, Wade MA, Ben Britton T, Buchanan C, Gardner L (2020) Mechanical and microstructural testing of wire and arc additively manufactured sheet material. *Mater Des* 192:108675. <https://doi.org/10.1016/j.matdes.2020.108675>
11. Michel L, Sanchez AMA, Silvestru V-A, Ariza I, Taras A, Angst U. Corrosion behaviour of point-by-point wire and arc additively manufactured steel bars. *Mater Corrosion.* (2022).
12. Silvestru V-A, Ariza I, Vienne J, Michel L, Aguilar Sanchez AM, Angst U, Rust R, Gramazio F, Kohler M, Taras A (2021) Performance under tensile loading of point-by-point wire and arc additively manufactured steel bars for structural components. *Mater Des* 205:109740. <https://doi.org/10.1016/j.matdes.2021.109740>
13. Huang C, Kyvelou P, Zhang R, Ben Britton T, Gardner L (2022) Mechanical testing and microstructural analysis of wire arc additively manufactured steels. *Mater Des* 216:110544. <https://doi.org/10.1016/j.matdes.2022.110544>
14. Mechtcherine V, Grafe J, Nerella VN, Spaniol E, Hertel M, Füssel U (2018) 3D-printed steel reinforcement for digital concrete construction—manufacture, mechanical properties and bond behaviour. *Constr Build Mater* 179:125–137
15. Laghi V, Palermo M, Tonelli L, Gasparini G, Ceschini L, Trombetti T. Tensile properties and microstructural features of 304L austenitic stainless steel produced by wire-and-arc additive manufacturing. *Int J Adv Manuf Technol.* (2020) 3693–3705. <https://doi.org/10.1007/s00170-019-04868-8>.
16. Haden CV, Zeng G, Carter FM, Ruhl C, Krick BA, Harlow DG (2017) Wire and arc additive manufactured steel: tensile and wear properties. *Addit Manuf* 16:115–123. <https://doi.org/10.1016/j.addma.2017.05.010>
17. Hadjipantelis N, Weber B, Gardner L (2021) Characterisation of the anisotropic response of wire and arc additively manufactured stainless steel. *Ce/Papers* 4:1757–1766
18. Hadjipantelis N, Weber B, Buchanan C, Gardner L (2022) Description of anisotropic material response of wire and arc additively manufactured thin-walled stainless steel elements. *Thin-Walled Structures.* 171:108634. <https://doi.org/10.1016/J.TWS.2021.108634>
19. PalmeiraBelotti L, van Nuland TFW, Geers MGD, Hoefnagels JPM, van Dommelen JAW (2023) On the anisotropy of thick-walled wire arc additively manufactured stainless steel parts. *Mater Sci Eng: A* 863:144538. <https://doi.org/10.1016/J.MSEA.2022.144538>
20. Laghi V, Tonelli L, Palermo M, Bruggi M, Sola R, Ceschini L, Trombetti T. Experimentally-validated orthotropic elastic model for wire-and-arc additively manufactured stainless steel. *Addit Manuf.* 42 (2021). <https://doi.org/10.1016/j.addma.2021.101999>.
21. Ermakova A, Mehmanparast A, Ganguly S, Razavi J, Berto F (2020) Investigation of mechanical and fracture properties of wire and arc additively manufactured low carbon steel components. *Theor Appl Fracture Mech* 109:102685. <https://doi.org/10.1016/J.TAFMEC.2020.102685>
22. Dinovitzer M, Chen X, Laliberte J, Huang X, Frei H (2019) Effect of wire and arc additive manufacturing (WAAM) process parameters on bead geometry and microstructure. *Addit Manuf* 26:138–146. <https://doi.org/10.1016/j.addma.2018.12.013>
23. Müller J, Grabowski M, Müller C, Hensel J, Unglaub J, Thiele K, Kloft H, Dilger K (2019) Design and parameter identification of wire and arc additively manufactured (WAAM) steel bars for use in construction. *Metals (Basel)* 9:725. <https://doi.org/10.3390/met9070725>
24. Aldalur E, Veiga F, Suárez A, Bilbao J, Lamikiz A (2020) High deposition wire arc additive manufacturing of mild steel: strategies and heat input effect on microstructure and mechanical properties. *J Manuf Process* 58:615–626. <https://doi.org/10.1016/J.JMAPRO.2020.08.060>
25. Laghi V, Palermo M, Bruggi M, Gasparini G, Trombetti T (2022) Blended structural optimization for wire-and-arc additively manufactured beams. *Progress Additive Manuf.* <https://doi.org/10.1007/s40964-022-00335-1>
26. Ou W, Mukherjee T, Knapp GL, Wei Y, DebRoy T (2018) Fusion zone geometries, cooling rates and solidification parameters during wire arc additive manufacturing. *Int J Heat Mass Transf* 127:1084–1094. <https://doi.org/10.1016/J.IJHEATMASSTRANSFER.2018.08.111>
27. Oliveira JP, Santos TG, Miranda RM (2020) Revisiting fundamental welding concepts to improve additive manufacturing: from theory to practice. *Prog Mater Sci* 107:100590. <https://doi.org/10.1016/J.PMATSCI.2019.100590>
28. Ron T, Levy GK, Dolev O, Leon A, Shirizly A, Aghion E (2020) The effect of microstructural imperfections on corrosion fatigue of additively manufactured ER70S-6 alloy produced by wire arc deposition. *Metals (Basel)* 10:98
29. VahediNemani A, Ghaffari M, Nasiri A (2020) On the post-printing heat treatment of a wire arc additively manufactured ER70S part. *Materials* 13:2795
30. Le VT, Dinh, Mai S, Quang, Hoang H (2020) A study on wire and arc additive manufacturing of low-carbon steel components: process stability, microstructural and mechanical properties. *J Brazilian Soc Mech Sci Eng* 42:480. <https://doi.org/10.1007/s40430-020-02567-0>
31. VahediNemani A, Ghaffari M, Nasiri A (2020) Comparison of microstructural characteristics and mechanical properties of ship-building steel plates fabricated by conventional rolling versus wire arc additive manufacturing. *Addit Manuf* 32:101086. <https://doi.org/10.1016/J.ADDMA.2020.101086>
32. Rafeezad M, Ghaffari M, VahediNemani A, Nasiri A (2019) Microstructural evolution and mechanical properties of a low-carbon low-alloy steel produced by wire arc additive manufacturing. *Int J Adv Manuf Technol* 105:2121–2134. <https://doi.org/10.1007/S00170-019-04393-8/FIGURES/10>
33. Ayan Y, Kahraman N (2021) Wire arc additive manufacturing of low-carbon mild steel using two different 3D printers. *Phys Met Metall* 122:1521–1529
34. Waqas A, Qin X, Xiong J, Zheng C, Wang H (2019) Analysis of ductile fracture obtained by charpy impact test of a steel structure created by robot-assisted GMAW-based additive manufacturing. *Metals (Basel)* 9:1208
35. Rafeezad M, Nemani AV, Ghaffari M, Nasiri A (2021) On microstructure and mechanical properties of a low-carbon low-alloy steel block fabricated by wire arc additive manufacturing. *J Mater Eng Perform* 30:4937–4945. <https://doi.org/10.1007/S11665-021-05568-9/FIGURES/6>
36. Relativity, [www.relativityspace.com](http://www.relativityspace.com), (n.d.).
37. MEGAROB Final Summary Report, <https://cordis.europa.eu/project/id/314015/reporting/es> (n.d.).
38. Nagasai BP, Malarvizhi S, Balasubramanian V (2022) Effect of welding processes on mechanical and metallurgical characteristics of carbon steel cylindrical components made by wire arc additive manufacturing (WAAM) technique. *CIRP J Manuf Sci Technol* 36:100–116. <https://doi.org/10.1016/J.CIRPJ.2021.11.005>
39. Papadakis EP, Papdakis EP, Stickels CA, Innes RC. An ultrasonic technique for measuring the elastic constants of small samples, *SAE Transactions.* (1995) 830–837.
40. Benschoter AO, Bramfitt BL (2004) Metallography and microstructures of low-carbon and coated steels. *Metallogr Microstruct* 9:588–607



41. DIN EN 10002–1:2001, Metallic materials - tensile testing, Metallic Materials - Tensile Testing, 54 (2001).
42. Laghi V, Palermo M, Gasparini G, Girelli VA, Trombetti T. On the influence of the geometrical irregularities in the mechanical response of wire-and-arc additively manufactured planar elements. *J Constr Steel Res.* 178 (2021). <https://doi.org/10.1016/j.jcsr.2020.106490>.
43. I.S. Organization, ISO 148–1 - Metallic materials - Charpy pendulum impact test - Part 1: Test method, 2016.
44. C.E.N. EN, 10025–2. Hot rolled products of structural steels—part 2: technical delivery conditions for non-alloy structural steels, Brussels, Belgium: European Committee for Standardisation. (2004).
45. UltraMag wire specifications, [https://www.lincolnelectric.com/assets/global/Products/ConsumableEU\\_MIGWires-ULTRAMAG-ULTRAMAG/ultramag-eng.pdf](https://www.lincolnelectric.com/assets/global/Products/ConsumableEU_MIGWires-ULTRAMAG-ULTRAMAG/ultramag-eng.pdf) (n.d.).
46. Vishnu PR. Solid-state transformations in weldments, welding, brazing, and soldering. (1993) 70–87. <https://doi.org/10.31399/ASM.HB.V06.A0001341>.
47. Thewlis G. Classification and quantification of microstructures in steels. 20 (2013) 143–160. <https://doi.org/10.1179/026708304225010325>.
48. Babu SS (2004) The mechanism of acicular ferrite in weld deposits. *Curr Opin Solid State Mater Sci* 8:267–278. <https://doi.org/10.1016/J.COSSMS.2004.10.001>
49. Bhadeshia HKDH. Bainite in Steels - transformations, microstructure and properties, second edition, IOM Communications Ltd, 2001.
50. Standard B (2006) Eurocode 3—design of steel structures—. BS EN 1993–1(1):2005
51. Tripathi U, Saini N, Mulik RS, Mahapatra MM (2022) Effect of build direction on the microstructure evolution and their mechanical properties using GTAW based wire arc additive manufacturing. *CIRP J Manuf Sci Technol* 37:103–109. <https://doi.org/10.1016/J.CIRPJ.2022.01.010>
52. E. 23 ASTM, Standard test methods for notched bar impact testing of metallic materials, E23–07a, Pennsylvania, PA, USA. (2007).
53. Lucon E, Lucon E, McCowan CN, Santoyo RL. Impact characterization of 4340 and T200 steels by means of standard, sub-size and miniaturized Charpy specimens, US Department of Commerce. *Nat Ins Standards Technol.* 2015.
54. Waqas A, Xiansheng Q, Jiangtao X, Chaoran Y, Fan L (2018) Impact toughness of components made by GMAW based additive manufacturing. *Procedia Structural Integrity* 13:2065–2070

**Publisher's note** Springer Nature remains neutral with regard to jurisdictional claims in published maps and institutional affiliations.